Observations of Arctic snow and sea ice cover from CALIOP lidar measurements

Xiaomei Lu, Yongxiang Hu, Zhaoyan Liu, Sharon Rodier, Mark Vaughan, Patricia Lucker, Charles Trepte, Jacques Pelon

Remote Sensing of Environment 194 (2017) 248–263

Contents lists available at ScienceDirect

Remote Sensing of Environment

journal homepage: www.elsevier.com/locate/rse

Observations of Arctic snow and sea ice cover from CALIOP lidar measurements

Xiaomei Lu [a,b,*], Yongxiang Hu [b], Zhaoyan Liu [b], Sharon Rodier [a,b], Mark Vaughan [b], Patricia Lucker [a,b], Charles Trepte [b], Jacques Pelon [c]

[a] Science Systems and Applications, Inc., Hampton, VA 23666, USA
[b] NASA Langley Research Center, Hampton, VA 23681, USA
[c] LATMOS, Universite Paris, (CNRS-UVSO), Paris 75005, France

ARTICLE INFO

Article history:
Received 3 November 2016
Received in revised form 23 March 2017
Accepted 30 March 2017
Available online 6 April 2017

Keywords:
Sea ice
Snow
CALIOP
Surface type identification

ABSTRACT

This paper describes the development and validation of a method to accurately identify snow/ice cover, surface melting, land surface and open water in polar regions using polar-orbiting Cloud-Aerosol Lidar with Orthogonal Polarization (CALIOP) lidar measurements from the Cloud and Aerosol Lidar and Infrared Pathfinder Observation (CALIPSO) mission. The technique is based on the relationship between integrated attenuated backscatter color ratio and integrated depolarization ratio, and is proven to efficiently separate snow/ice cover and surface melting from open water and land surfaces. The method has been applied to 10 years (2006–2016) of CALIOP data to study the seasonal and inter-annual variability of Arctic sea ice cover and its declining trend. Results show that the area fraction of snow cover over land at latitudes >60°N varied between 0.9 during winter and 0.1 in summer. The CALIOP observations of Arctic sea ice cover exhibit a strong seasonal cycle and significant inter-annual variability, which are consistent with the passive microwave-based sea ice results. The >10 years of CALIOP continuous observations of the snow/ice cover will benefit the communities modeling snow/ice melting and climate change.

1. Introduction

Over 30% of the Earth's land surface is seasonally covered by snow, and 10% is permanently covered by glaciers (Dozier, 1989; Lemke et al., 2007; Wolff, 2013). Snow and ice play important interactive roles in the Earth's radiation balance, because they have a higher albedo than any other natural surface. Fresh snow reflects up to 80% or more of the incoming solar energy, which compares drastically with only 20% or less for bare ground (König et al., 2001). The most notable positive feedback is the sea ice albedo feedback, which results from the large contrast between the albedos of sea ice (>0.6) and open water (~0.07) (Perovich et al., 2007). Due to the Arctic temperature rise, the ice or the overlying snow cover of high albedo is increasingly replaced with open water or bare soil of lower albedo. This results in additional absorption of solar radiation, which accelerates further snow/ice loss. However, understanding the interaction of solar energy with the ice cover is a complex task. First, it is not easy to determine how much solar energy is reflected/or absorbed by the ice and how much is subsequently transmitted into the ocean. Second, the seasonal evolution of the ice albedo depends on the characteristics of the snow cover in spring and melt ponds in summer (Perovich et al., 2002; Perovich and Polashenski, 2012). For example, in summer time, the surface conditions in the Arctic can vary from deep snow, to bare ice, to melt ponds, to open leads within small areas that are often <1 km^2 (Perovich et al., 2002) and to bare or grass soils. These surface types have different physical and optical properties and interact with the incoming solar energy differently. Because of the importance of the sea ice albedo feedback mechanism, the ability to identify different surface types at fine spatial scales is important for predicting snow and ice melt as well as for understanding the ice extent loss, which in turn affects the global energy budget and therefore climate.

Satellites are proven to be well suited to measure snow/ice cover because the high reflective nature of snow/ice at visible wavelengths presents a good contrast with other natural surface covers. For example, the NASA Earth Observing System (EOS) MODerate-Resolution Imaging Spectroradiometer (MODIS) instruments on the Terra and Aqua satellites identify snow cover based on a Normalized Difference Snow Index (NDSI) spectral band ratio, which is the difference of reflectances in a visible band and a shortwave infrared band divided by the sum of the two refectances (Hall and Riggs, 2007; Hall et al., 2002). The NDSI

* Corresponding author at: Science Systems and Applications, Inc., Hampton, VA 23666, USA.
E-mail address: xiaomei.lu@nasa.gov (X. Lu).

http://dx.doi.org/10.1016/j.rse.2017.03.046

approach takes advantage of the fact that snow reflectance is high in the visible wavelengths and has low reflectance in the shortwave infrared wavelengths (Hall and Riggs, 2007; Parajka et al., 2012).

The polar-orbiting Cloud-Aerosol Lidar with Orthogonal Polarization (CALIOP) has been providing continuous global measurements at two-wavelengths (532 and 1064 nm) between 82°S and 82°N since June 2006 (Winker et al., 2010). These valuable datasets can be used to study the snow and sea ice cover in the Arctic where in-situ observations are relatively rare due to the extreme weather conditions in high latitudes. In contrast to MODIS passive remote sensor that can only provide useful surface type measurements during daylight seasons and are not reliable at low solar angles, the CALIOP lidar makes reliable measurements both day and night, and at low solar angles through considerable aerosol loads and thin clouds (Behrenfeld et al., 2013; Josset et al., 2012). The CALIOP lidar has a 70 m footprint on the Earth's surface that is sampled along track every 333 m. The advantage of using CALIOP measurements is that the CALIOP has a small sample footprint size compared to passive sensors.

In this paper, we develop a new retrieval method for surface type identification in the Arctic that is based upon the relationship between CALIOP's integrated attenuated backscatter color ratio and integrated depolarization ratio. In Section 2 we present CALIOP observations of integrated attenuated backscatter color ratio and depolarization ratio, and describe other datasets used in this paper. The surface type separation method and its application to 10 years of the CALIOP Arctic sea ice measurements are described in Sections 3 and 4. The results from CALIOP measurements shown in this study are compared with datasets from both MODIS and passive microwave sensors measurements. Section 5 gives the summary and conclusions.

2. Data products

2.1. CALIOP level 1 data products

CALIOP flies aboard the Cloud-Aerosol Lidar and Infrared Pathfinder Satellite Observation (CALIPSO) satellite, which deploys both active and passive sensors designed for atmospheric cloud and aerosol research. CALIOP is the first space-borne polarization-sensitive lidar (with cross-polarization and co-polarization channels at 532 nm) to provide vertical profiles of the elastic backscattering from a near nadir-viewing during both day and night between 82°N and 82°S (Hunt et al., 2009; Winker et al., 2009). In this paper, we use the new CALIOP level 1 version 4 data product to derive the integrated attenuated backscatter that is a major parameter used in the surface type identification method described in Section 3. Because the CALIOP lidar receiver's transient response yields a long tail in the attenuated backscatter profile below the

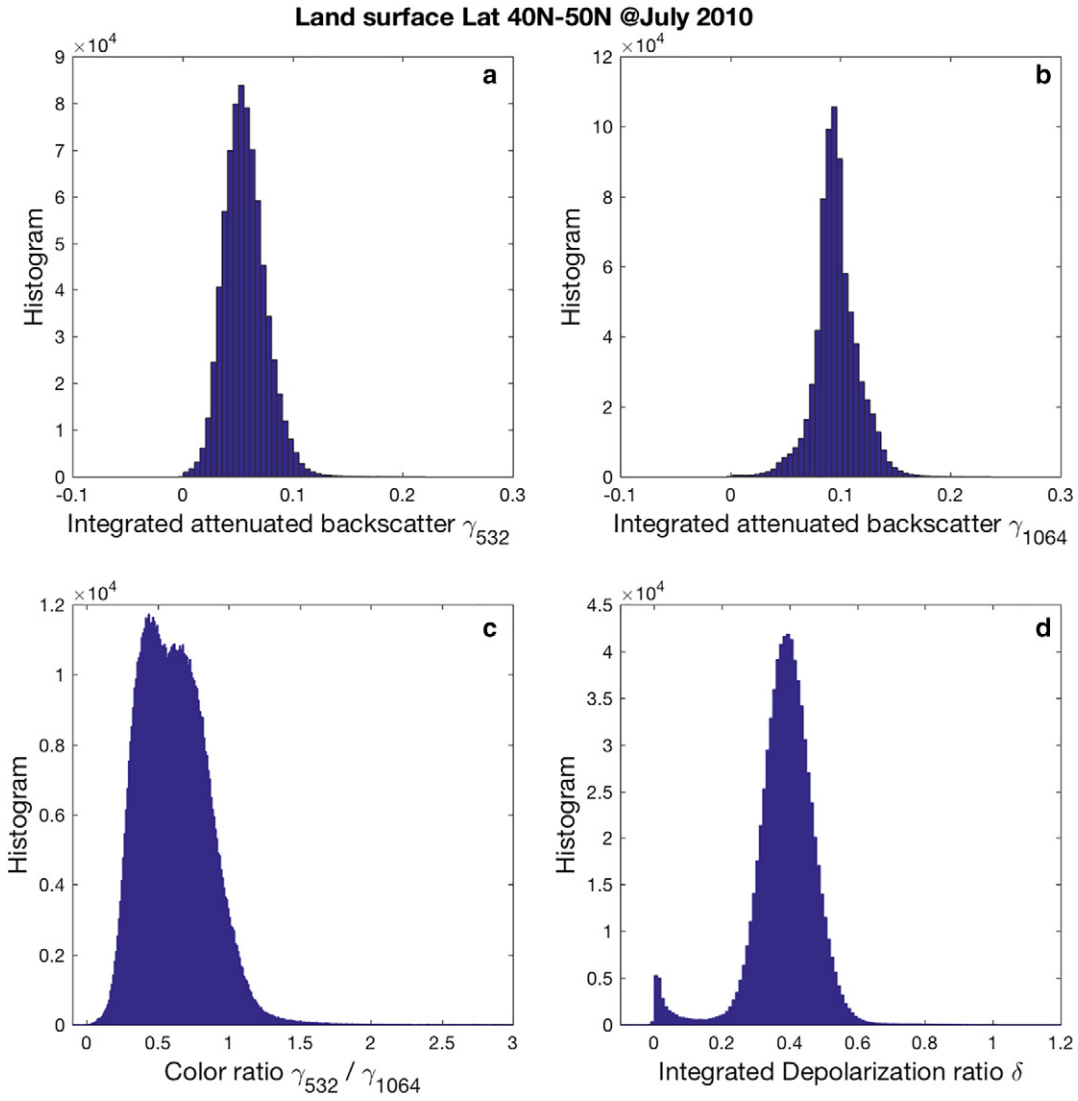

Fig. 1. Histogram of land surface integrated attenuated backscatter γ_λ at 532 nm (a), 1064 nm (b), color ratio x (c) and depolarization ratio δ (d).

surface return (Hu et al., 2007; Hunt et al., 2009; Lu et al., 2014), the integration is performed between 30 m above and 300 m below the surface. The surface is determined to be the maximum lidar attenuated backscatter at 532 nm located within 150 m above or below the surface elevation reported by the Global 30 Arc-Second (GTOPO30) Digital Elevation Model (DEM) (https://lta.cr.usgs.gov/GTOPO30). The surface integrated attenuated backscatter (unit: sr^{-1}) is calculated using,

$$\gamma_\lambda = \frac{\int_{\text{surface}-300\text{m}}^{\text{surface}+30\text{m}} \beta'_\lambda(z)\mathrm{d}z}{T_\lambda^2} \quad (1)$$

with the surface attenuated backscatter coefficients, $\beta'_\lambda(z)$, obtained directly from CALIOP level 1 data products. T^2 is the two-way atmospheric transmittance derived from meteorological data reported in the CALIOP level 1 files, and λ is the wavelength (532 nm and 1064 nm for the CALIOP lidar). For this study, we only analyze cases under clear sky conditions, so that the T^2 term provides an accurate estimate of the total signal attenuation between the lidar and the Earth's surface. In this paper, for a single-shot lidar profile if its integrated attenuated backscatter (IAB) at 532 nm of the column above the surface is lower than 0.017/sr, this single-shot profile is determined as clear (Lu et al., 2016). The use of IAB <0.017/sr warrants the air column is sufficiently clear (Josset et al., 2010a; Lu et al., 2016) so that the surface return is minimally perturbed by a reduction in atmospheric transmission due to haze or semi-transparent clouds. The integrated attenuated backscatter color ratio is defined as the ratio of the integrated attenuated backscatter at two wavelengths, $\chi = {}^{\gamma 532\text{nm}}/\gamma_{1064\text{nm}}$. The integrated depolarization ratio at 532 nm is.

$$\delta = \frac{\gamma_\perp}{\gamma_\parallel} \quad (2)$$

where $\gamma_\perp$ and $\gamma_\parallel$ are integrated attenuated backscatter from the cross-polarization and co-polarization channels at 532 nm by Eq. (1). It is noted from Eq. (2) that depolarization ratio is not depending on transmission for haze or semi-transparent clouds (Hu et al., 2008). The CALIOP level 1 version 4 dataset used in this study was taken from June 2006 to June 2016, comprising 10 years of lidar measurements. CALIOP observations indicate that there are about 50% of nearly clear sky cases (with IAB < 0.017/sr) in the Arctic region on a yearly average. The results shown below are derived from both daytime and nighttime data.

2.2. AMSR-E daily sea ice concentration

The Advanced Microwave Scanning Radiometer (AMSR-E/Aqua) level 3 grided product at 12.5 km spatial resolution provides a daily averaged sea ice concentration (0–100%) for both north and south polar regions (Markus et al., 2011). The sea ice concentration product is generated using the Enhanced NASA Team (NT2) algorithm, which calculates the sea ice concentration using the individual level 2-A swaths rather than using gridded averaged brightness temperatures. This is done in order to make the atmospheric corrections on an orbit by orbit basis before obtaining daily average ice concentrations (Markus

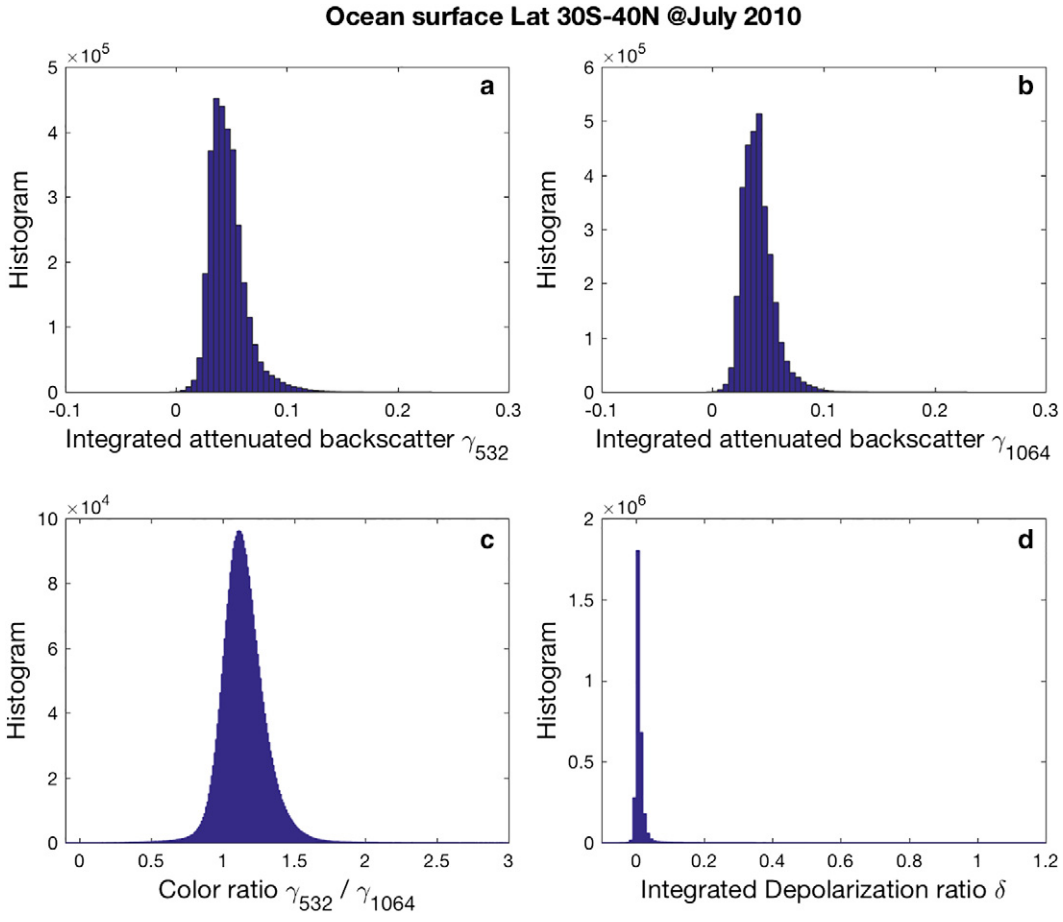

Fig. 2. Histogram of open water integrated attenuated backscatter γ_λ at 532 nm (a), 1064 nm (b), color ratio x (c) and depolarization ratio δ (d).

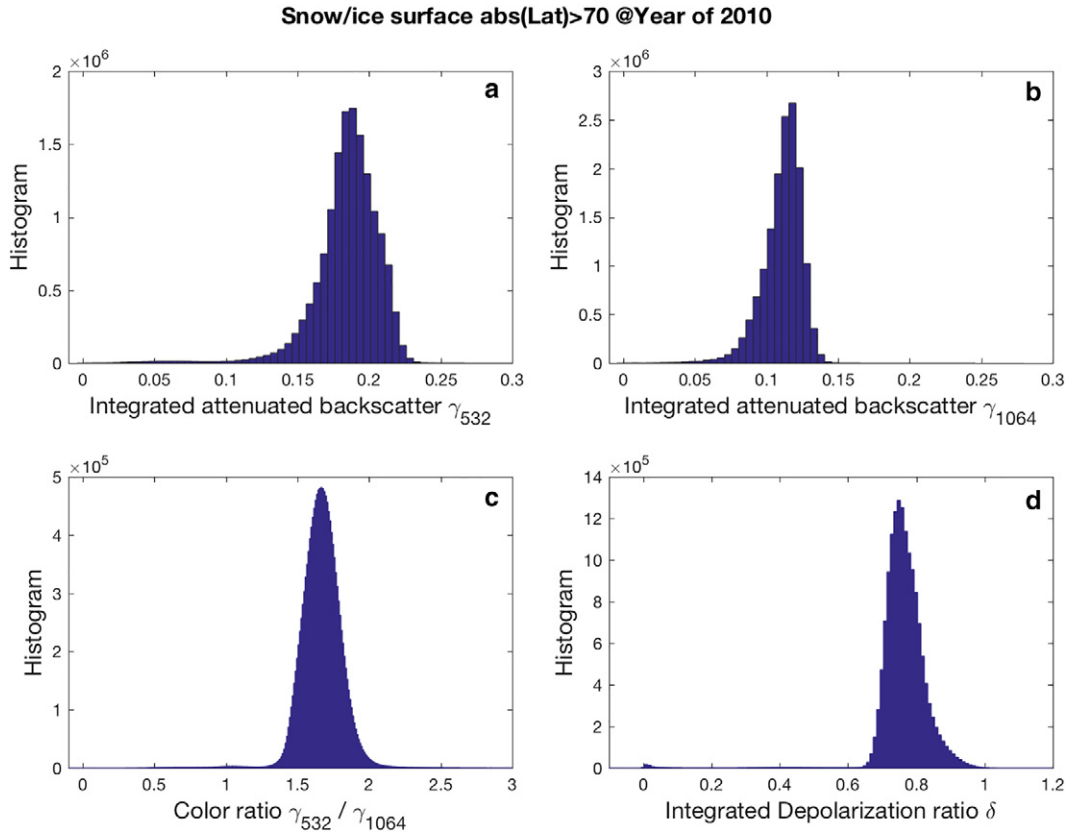

Fig. 3. Histogram of snow/ice integrated attenuated backscatter γ_λ at 532 nm (a), 1064 nm (b), color ratio x (c) and depolarization ratio δ (d).

and Cavalieri, 2000). The temporal coverage of the data products are from 1 June 2002 through 4 October 2011 because the AMSR-E mission launched on 2 May 2002 and ended in 04 December 2011 (Cavalieri et al., 2014). Information about the sea ice concentration allows us to assess the sea ice area and extent changes.

2.3. MODIS snow cover

In this study, we make use of the MODIS/Aqua snow cover monthly L3 Climate Modeling Grid (CMG) data set version 5 (MYD10CM), which is available from the National Snow and Ice Data Center (NSIDC) (Hall et al., 2007; Hall et al., 2002). This study only uses data with good quality, when the quality assessment (QA) flag is zero.

2.4. SMMR and SSM/I-SSMIS sea ice data

The National Snow and Ice Data Center (NSIDC) distributes several data sets for ice-covered area and extent, which provide users with information about sea ice extent, total ice-covered area, ice persistence, and monthly climatologies of sea ice concentrations (http://nsidc.org/data/smmr_ssmi_ancillary/index.html). These data sets are derived from the Scanning Multichannel Microwave Radiometer (SMMR), the Special Sensor Microwave/Imager (SSM/I), and the Special Sensor Microwave Imager/Sounder (SSMIS) using the NASA Team and Bootstrap algorithms, and are provided by the NASA Goddard Space Flight Center (GSFC) (Fetterer et al., 2016; Stroeve, 2003). The sea ice trends products from November 1978 to August 2016 derived from the NASA team sea ice concentrations (referred to as NASA team dataset hereafter) are used in this study.

Table 1
Typical values of integrated attenuated backscatter, depolarization ratio and color ratio for snow/ice, open water and land surfaces obtained from CALIOP measurements.

	Snow/ice	Open water	Land
$\gamma_{532\ nm}$ (/sr)	0.19 ± 0.02	0.05 ± 0.02	0.06 ± 0.02
$\gamma_{1064\ nm}$ (/sr)	0.11 ± 0.01	0.04 ± 0.01	0.09 ± 0.02
δ	0.77 ± 0.08	0.01 ± 0.01	0.38 ± 0.09
$\gamma_{532\ nm}/\gamma_{1064\ nm}$	1.73 ± 0.16	1.15 ± 0.15	0.62 ± 0.24

3. Method

Presented in Fig. 1 are the land surface integrated attenuated backscatter γ_λ, depolarization ratio δ and color ratio χ, calculated using the CALIOP nighttime data in July 2010 measured between 40°N and 50°N. The ocean surface results in Fig. 2 are calculated between latitudes from 30°S to 40°N, and the snow/ice surface results in Fig. 3 are calculated in 2010 at latitudes north of 70°N or south of 70°S. In Figs. 1, 2 and 3,

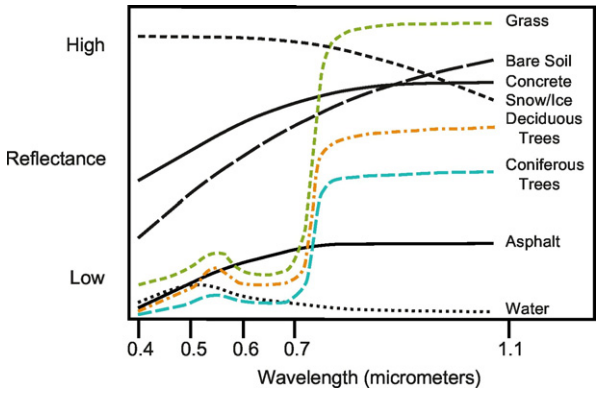

Fig. 4. Spectral reflectance curves for different land surface covers (Fig. 4.04 of Goetz and Huemmrich, 2003).

the International Geospherre-Biosphere Programme (IGBP) land surface classification was used to help identify the surface type as water bodies (IGBP = 17) or permanent snow and ice (IGBP = 15) (http://ceres.larc.nasa.gov/science_information.php?page=CeresSurfID) to characterize CALIOP lidar returns from these surfaces. The IGBP surface types used here and for CALIPSO are the same as those used in the Clouds and the Earth's Radiant Energy System /Surface and Atmospheric Radiation Budget (CERES/SARB) surface map, which are representative of biome types observed during 2000 and are not intended for the study of land use changes over time but offer a snapshot of the Earth's surface [https://ceres.larc.nasa.gov/science_information.php?page=CeresSurfID]. However, there is IGBP surface type misclassification near coasts (Josset et al., 2010b). Typical mean values of integrated attenuated backscatter, depolarization ratio and color ratio for snow/ice, open water and land surfaces are given in Table 1. They are consistent with the spectral reflectance of green vegetation and other land covers shown in Fig. 4 (Goetz and Huemmrich, 2003). The land surface results in Table 1 agree with the averaged reflectance spectra for different land cover types obtained by the albedometers (e.g. reflectance is <0.2 in the visible and higher than 0.3 in the near-infrared) (Liang et al., 2003). The snow/ice results are in good agreement with the sea ice reflectance (i.e. around 0.8 in the visible and lower values in the near-infrared, Winther et al., 2004) and agree with the snow spectral reflectance (varying from approximately 0.8 in the visible to lower than 0.6 in the near-infrared, Gao et al., 1998; Warren, 1982).

The characteristic values for the snow/ice color ratio and depolarization ratio are 1.60 ± 0.17 and 0.77 ± 0.07, respectively, as shown in Fig. 3. However, the measured reflectance will decrease as the snow melts during summer and increase as a result of new snowfall in winter. Other land surface covers, such as bare soil, grass, trees, concrete, or asphalt without snow/ice cover generally show a steady rise in reflectance as wavelength increases from the visible to the near infrared as shown in Fig. 4, which results in the mean color ratio of these land surfaces being lower than 1 (around 0.62 ± 0.24). The depolarization ratio distribution of land surface in Fig. 1d shows two modes, one with basically no depolarization and another one with a much higher frequency centered near 0.38 ± 0.09. The low depolarization ratio values are mainly from coastal areas, and are likely mix land and water surfaces where the IGBP may have misclassified the surface type as land. As the CALIOP lidar system is pointing at near-nadir angle (0.3° or 3°), specular reflectance from the ocean surface is the dominant contributor to the integrated attenuated backscatter compared with the contributions from subsurface and whitecaps (Josset et al., 2010c; Lu et al., 2014), and this produces small values (<0.05) of integrated depolarization ratio as shown in Fig. 2d.

Fig. 5a, b and c show 2-D histograms of depolarization ratio and color ratio for open water, land and snow/ice surfaces identified based on the IGBP surface types. The colors in the figure represent the number of CALIOP observations. The clusters of low depolarization ratio values around 0 shown in Fig. 5b and c are likely to be water surfaces (color ratio close to 1.1 as in Fig. 5a) that are misclassified by the IGBP (Josset et al., 2010b). The mean values of depolarization ratio and color ratio for different IGBP surface types are given in Fig. 5d. The large spatial separation of the histograms shown in Fig. 5 indicate that

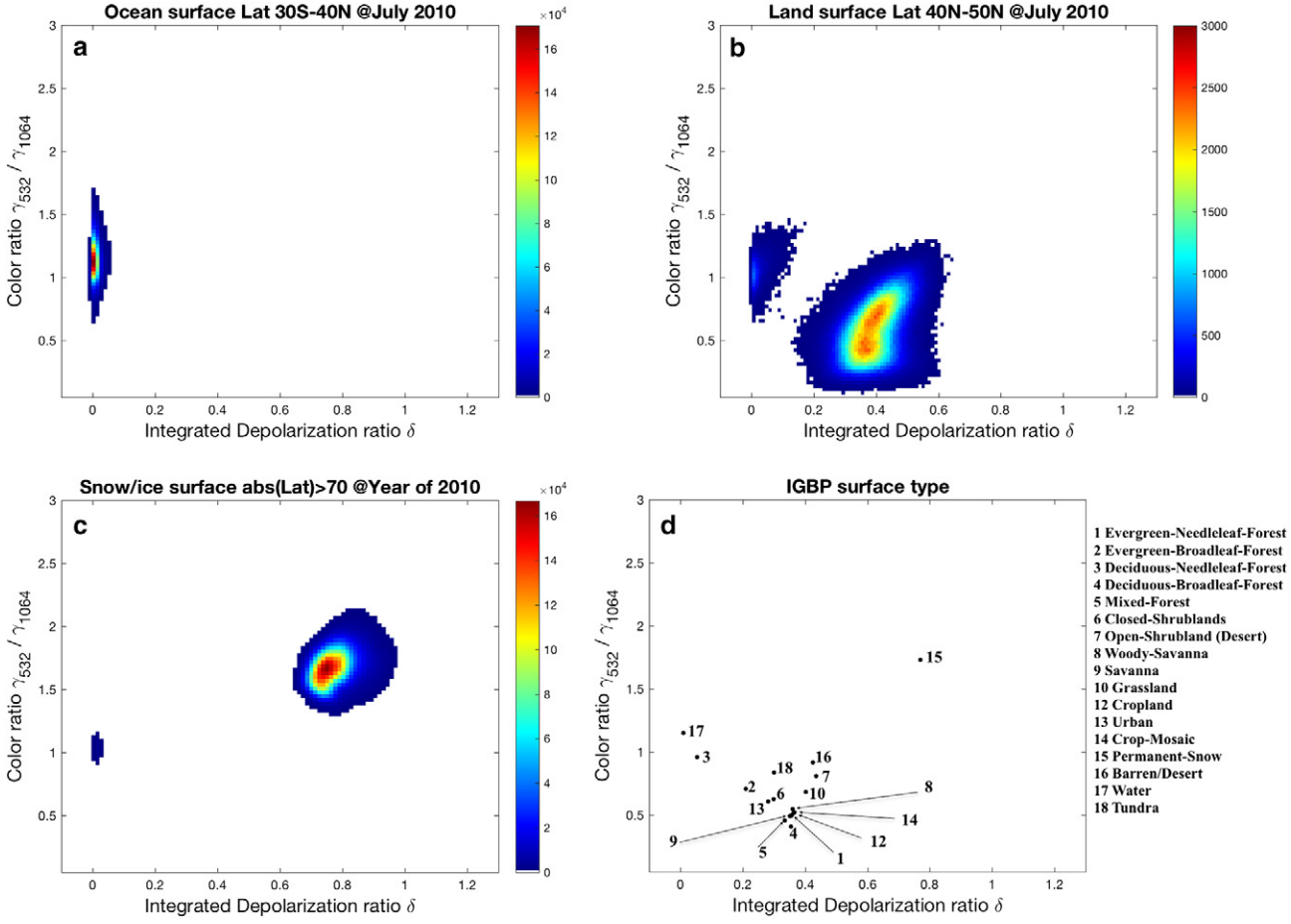

Fig. 5. 2-D histogram of depolarization ratio and color ratio for open water (a), land (b) and snow/ice surfaces (c). The color bar shows the number of CALIOP lidar observations. (d) mean values of depolarization ratio and color ratio for different IGBP surface types. The labeled number is the IGBP surface type index as the legend shown on right.

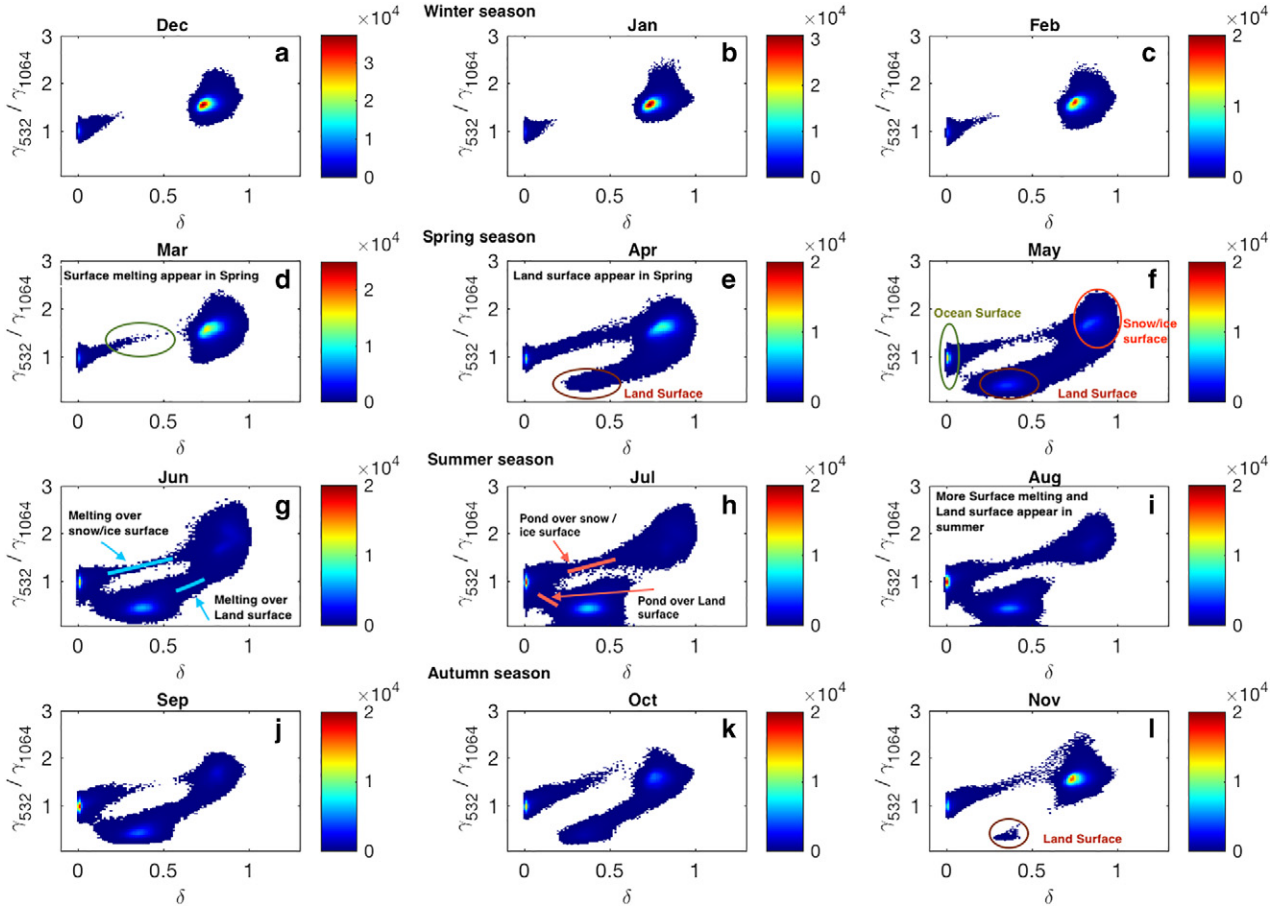

Fig. 6. Monthly distribution of 2-D histogram of depolarization ratio and color ratio as a function of season (winter: a, b, c; spring: d, e, f; summer: g, h, i; and autumn: j, k, L). Note that December 2010 is used to begin the winter season.

we can accurately separate snow/ice, open water and land surfaces through the relation between color ratio and depolarization ratio measured by CALIOP.

Fig. 5 shows that the snow/ice surface type typically has higher depolarization ratio and color ratio values than the open water and land surfaces. Using a similar classification, Fig. 6 shows the 2-D histogram of the relation between depolarization ratio and color ratio at latitudes north of 60°N depicting the seasonal evolution of the surface conditions in the Arctic in 2010. Changes in color ratio and depolarization ratio can thus be used as an indicator of surface melting as detailed in Fig. 6. During the Arctic winter, there are only snow/ice and open water modes, and the snow/ice mode is the dominant surface type (Fig. 6a, b and c). There is almost no bare ground. As a result, there is no a land surface mode during the winter months. As the season progresses into early spring, a transition zone appears between the snow/ice and open water modes, due to the melting of some sea ice or snow over the sea ice (green circle in Fig. 6d). Meanwhile, there is no clear indication of snow/ice melting over land. As the air warms up further, a land mode emerges in April (brown circle in Fig. 6e), indicating that snow/ice are completely melted over some land surfaces and bare ground begins to appear. Moving into the summer months, most snow/ice cover has melted and the land mode becomes the strongest while the snow/ice mode becomes the weakest. Still, a weak snow/ice mode remains throughout the summer months (Fig. 6g, h and i), corresponding to the permanent snow/ice cover. There also appear to be transition zones between the land and snow/ice modes, and the land and open water modes, as the air temperature increases. As the surface melting increases, melt ponds can form rapidly either over ice surfaces (the transition zone between the snow/ice and open water modes) or over land surfaces (the transition zone between the land and open water modes) as indicated by the two red lines shown in Fig. 6h. The transition zone between the snow/ice and land mode corresponds to land surfaces which are covered with the broken snow and ice (Fig. 6g). After summer, the ground and open seas start to freeze and the snow/ice cover becomes larger as winter approaches. However, the bare ground can be still seen until November (cases within brown circle in Fig. 6L). From Fig. 6 we can see that the Arctic surface is characterized by a highly reflective snow/ice cover with a little open water present in winter. The surface starts to melt in spring. The surface type in summer is a mixture of melting snow, bare ice and melt ponds. The melt ponds, flooded surfaces or wet surfaces are all classified as surface melting here. In fall, the

Table 2
Threshold values used in clear sky conditions to identify the snow/ice cover and surface melting from open water and land surfaces in Arctic region at latitudes above 60°N.

	$\gamma_{532\ nm}$ (/sr)	δ	$\gamma_{532\ nm}/\gamma_{1064\ nm}$
Open water	<0.1	<0.15	<1.5
Snow/ice melting over sea ice	0.06–0.1	0.15–0.65	>1
Snow/ice cover	>0.1	>0.65	>1.3
Land surface	<0.1	0.2–0.6	<1
Snow/ice melting over land	0.06–0.15	>0.6	0.6–1.3

surface starts to freeze and return back to its winter condition. One can see in Fig. 6j that the sea ice occurrence is minimal in September.

Fig. 6 shows that the differences between snow/ice, surface melting, land surface and open water are significant. As a result, we can separate the snow/ice cover and surface melting from open water and land surface using the CALIOP measurements. Since snow/ice reflects more energy in the visible region than in the near infrared, the color ratio between 532 nm and 1064 nm enhances the contrast between snow/ice and bare ground. Additionally, the depolarization ratio of snow/ice remains high compared with that of bare ground and open water. From the frequency distributions shown in Figs. 3, 5 and 6, snow/ice covered surface is identified when the color ratio is higher than 1.3 and depolarization ratio higher than 0.65. However, if the integrated attenuated backscatter at 532 nm is lower than 0.1/sr, then the case will not be identified as snow/ice even if the other criteria are met. This prevents cases containing very dark targets such as water near coastlines and black spruce forest, from being identified as snow/ice. For the clear sky cases considered here, surface melting in the Arctic sea ice region was identified whenever the depolarization ratios were between 0.15 and 0.65, the $\gamma_{532\ nm}$ were between 0.06 sr^{-1} and 0.1/sr and the color ratios were >1. For surface melting over sea ice, a color ratio >1 is consistent with spectral albedo shape of melt ponds, which have higher albedos across the visible from 400 to 600 nm and lower albedos in the near infrared at wavelengths beyond 750 nm where the in-water absorption is so great that the underlying ice does not contribute to the albedo (Perovich et al., 2002). The threshold values used to

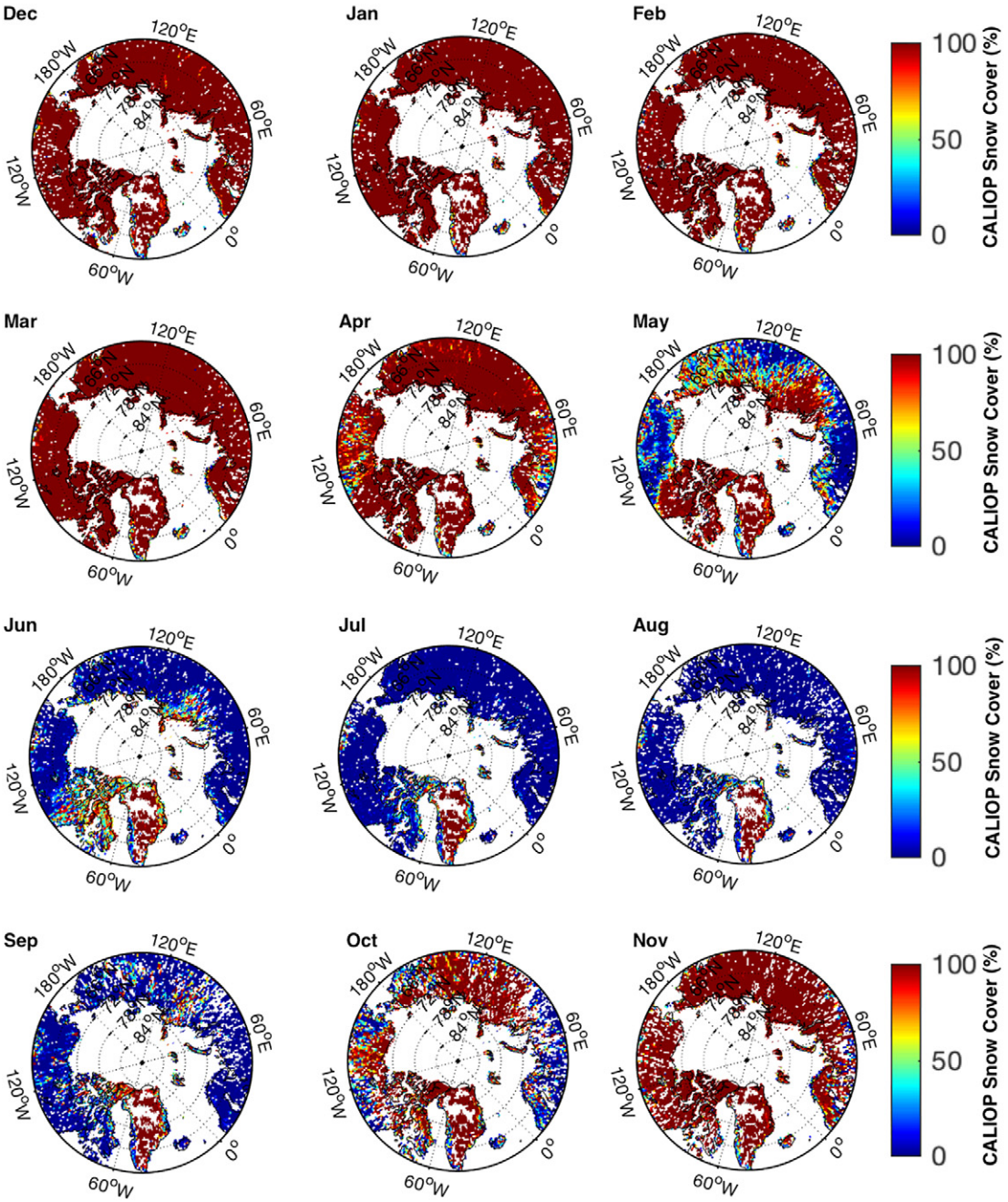

Fig. 7. CALIOP snow/ice cover (%) over land surface in different months.

identify snow/ice covered surfaces, open water and surface melting over the Arctic region are summarized in Table 2.

4. Validation

4.1. Snow/ice surface

The aim of this section is to validate the CALIOP surface identification results retrieved by the proposed threshold method. It is easy to discriminate snow/ice surfaces from the surrounding open water, wet surface and bare ground based on the threshold values in Table 2. Fig. 7 shows the monthly distribution of CALIOP snow/ice cover percentage (0–100%) above 60°N in 2010, which is calculated as the ratio between CALIOP snow/ice observations and total CALIOP observations within 0.5° by 1° latitude and longitude grid cell. The white pixels in Fig. 7 represent missing data, which are primary due to cloud/aerosol atmospheric conditions where the IAB exceeds 0.017/sr. There is a good overall agreement between the CALIOP snow/ice cover and the MODIS/Aqua monthly snow cover over land surfaces shown in Fig. 8 with a correlation coefficient of 0.92. We note that during January, February, November and December, the MODIS polar overpasses occur during nighttime when the required observations at visible wavelengths cannot be made at higher latitude. This fact explains the missing snow cover that is apparent in Fig. 8 over land surfaces during these months.

This comparison shows (see Figs. 7 and 8) that the CALIOP threshold algorithm works quite well in snow/ice cover identification. Moreover,

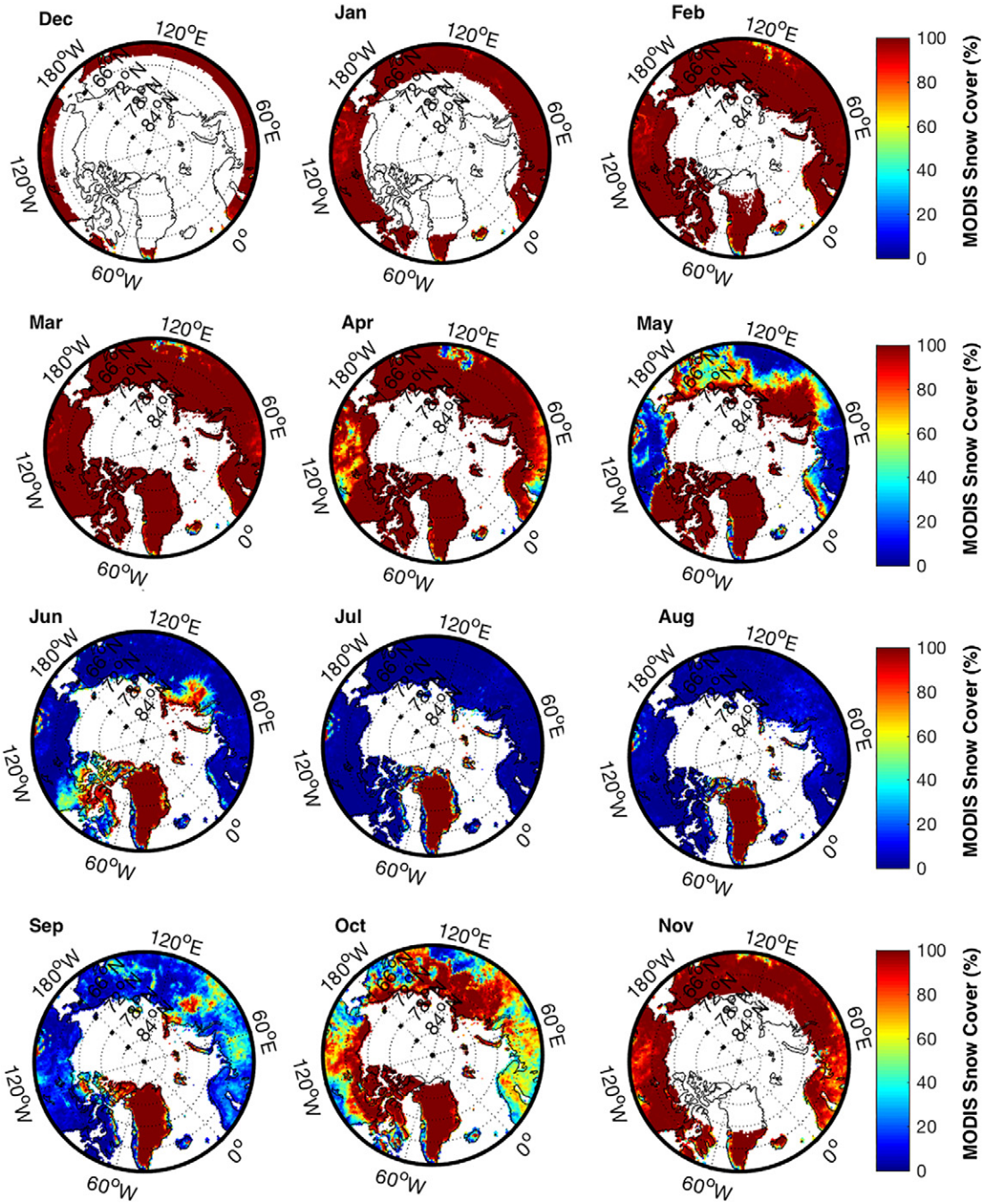

Fig. 8. MODIS–Aqua snow cover (%) in different months.

compared with the MODIS data products missing snow cover during nighttime as shown in Fig. 8, the CALIOP lidar can provide snow/ice data sets during both daytime and nighttime (Fig. 7).

The probability of Arctic sea ice cover (%) simply takes the percentage of snow/ice observed by the threshold method as the fraction of the total CALIOP observations in a 0.5° by 1° latitude and longitude grid cell. Fig. 9 shows monthly distributions of the Arctic sea ice cover observed by CALIOP in the year of 2010. The large scale variations in CALIOP Arctic sea ice cover probability (0–100%) show a pattern that is similar to that of AMSR-E sea ice concentration (0–100%) shown in Fig. 10. Generally, a high sea ice concentration is found in all seasons at latitudes above 84°N, as shown in Fig. 10. The results of Figs. 9 and 10 indicate that the sea ice cover probability or concentration is low in summer and early fall but high in winter and spring at relatively low latitude (e.g. latitude < 78°N). This is because the sea ice of that region melts during the summer time and reforms in winter. Various measurements from the Surface Heat Flux of the Arctic Ocean (SHEBA) experiment show that melt onset is primarily due to large increases in the downwelling longwave radiation and modest decreases in the surface albedo (Persson and Ola, 2012). Once melt onset over Arctic sea ice is initiated, the sea ice albedo decreases, resulting in the shortwave radiation becoming a strong amplifying factor to surface warming and melting of the sea ice cover (Mortin et al., 2016).

The area fraction of snow/ice cover is defined as the ratio between areas with snow/ice cover percentage >80% and total land surface areas at latitudes above 60°N. The left panel of Fig. 11 shows the

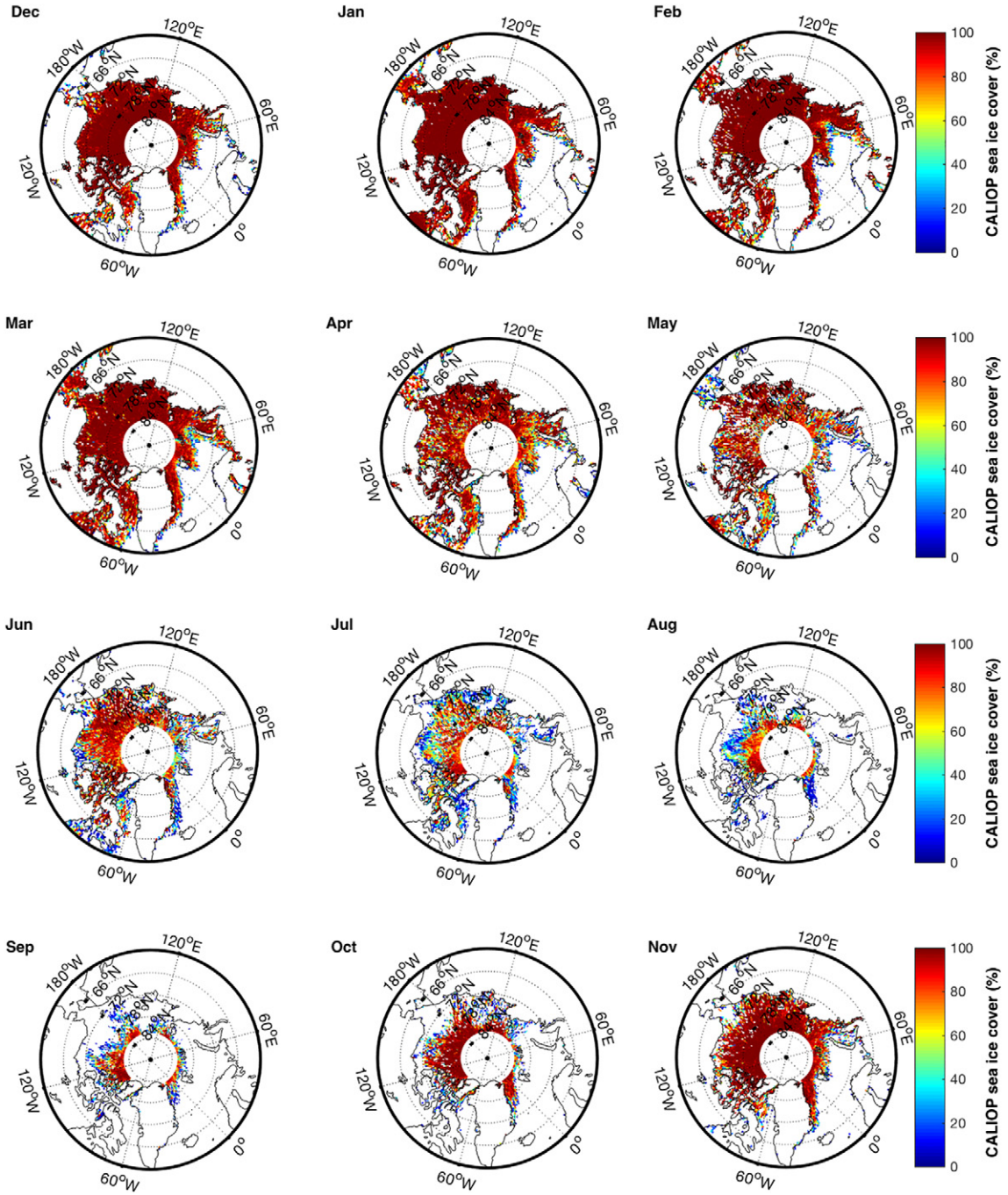

Fig. 9. Probability of Arctic sea ice cover (%) observed by CALIOP lidar in 2010.

monthly area fraction (%) of snow/ice cover over land observed by both CALIOP and MODIS instruments and Table 3 gives the area fraction values in four seasons. The left panel of Fig. 11 indicates that the area fraction of snow cover at latitudes >60°N varied between 0.9 during winter to 0.1 in summer. It is encouraging that the agreements in the averaged area fractions are within a few percent, and have a root mean squared error of 3.5% with a coefficient of determination (R^2) of 0.99. The results indicate that there is potential to accurately monitor snow/ice cover in the Arctic using CALIOP lidar data, which can provide observations during both daytime and nighttime.

The area fraction (%) of Arctic sea ice cover is the ratio between areas with sea ice probability or concentration >15% and total areas over ocean regions. The definition of Arctic open water area fraction is the same as sea ice area fraction with open water retrieved by the threshold method shown in Table 2. The right panel of Fig. 11 shows the monthly area fractions of CALIOP-retrieved and AMSR-E retrieved sea ice cover and CALIOP-retrieved open water area fraction in 2010. Averaged area fractions of sea ice cover and open water in each of the four seasons are given in Table 3. Significant changes occur in the sea ice cover during the summer melt season, as the results in Figs. 9, 10 and 11 illustrate. During winter and spring, the area fraction of sea ice cover can be as high as 76% while the open water is as low as 15% (right panel of Fig. 11). The peak open water area fraction in September exceeded 50% (green line in right panel of Fig. 11). The amount of surface melting over the Arctic sea ice surface in summer and fall seasons, ranges between 3% and 6% of the total area. Please note that the cases changing

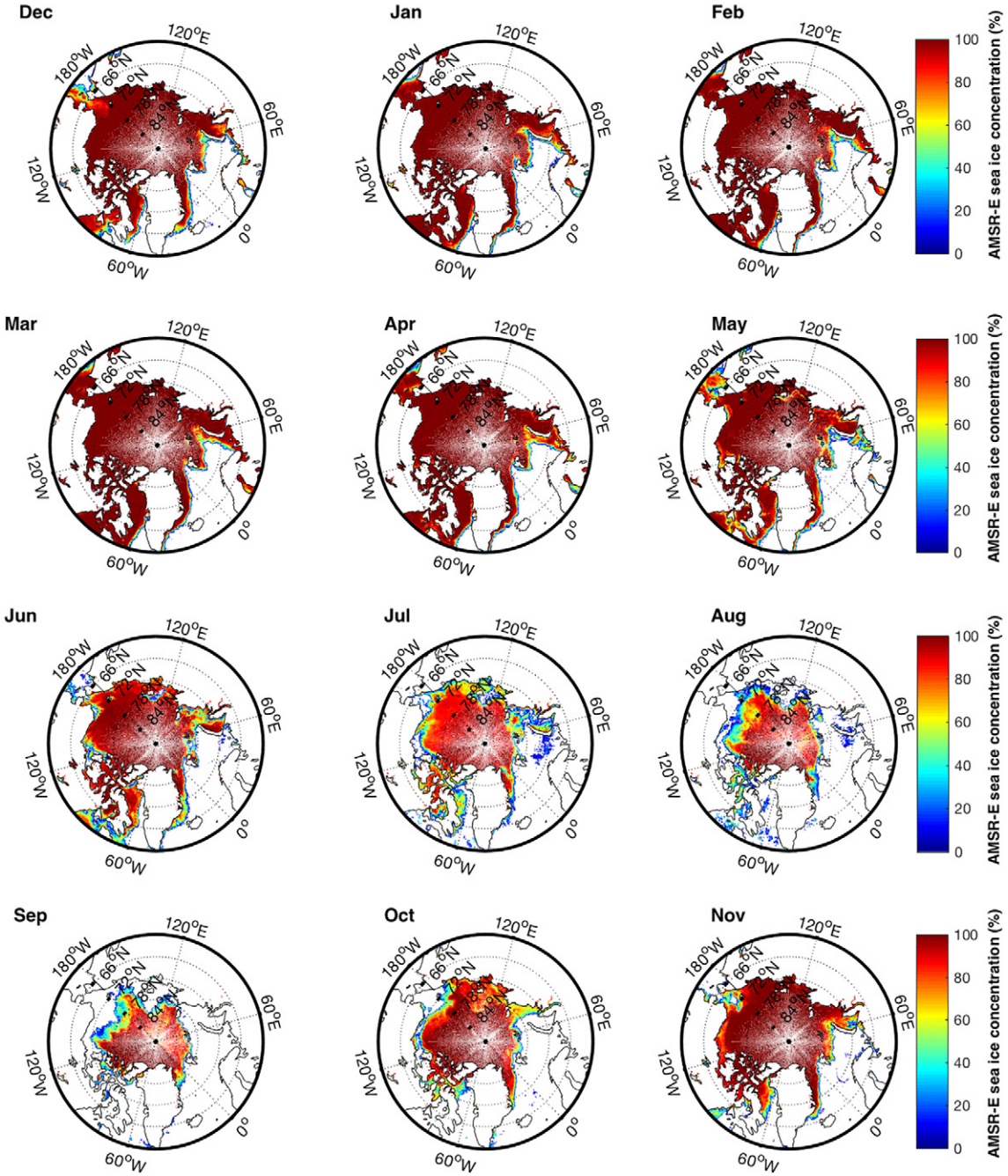

Fig. 10. Monthly distribution of AMSR-E sea ice concentration (%) in 2010.

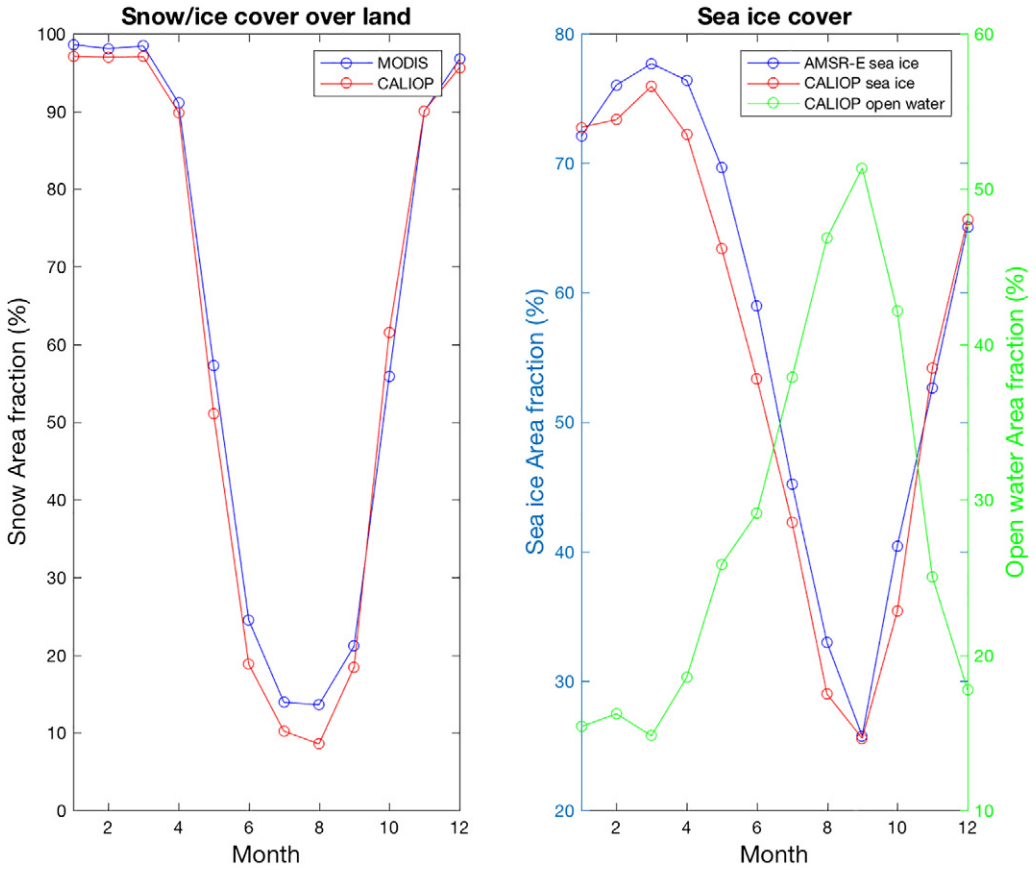

Fig. 11. Monthly snow/ice cover area fraction (left panel), sea ice and open water area fraction (right panel) in 2010.

from sea ice cover to open water (totally melted) are considered to be open water cases (not surface melting) in summer and fall, which makes the area fraction of surface melting smaller here. The area fraction of sea ice cover retrieved from CALIOP data shows a root mean squared difference of 3.6% compared to those from AMSR-E sea ice datasets with coefficient of determination (R^2) of 0.96. As shown in Fig. 11, the CALIOP area fraction retrievals are slightly lower (2%–6%) than AMSR-E based values, which may be attributed to a small number of tracks in the selected CALIOP latitude–longitude grid cell (0.5° × 1°) and rejecting data where the IAB exceeds 0.017/sr identified as cloud/aerosol.

As illustrated in Figs. 12 and 13, the 10 years of Arctic sea ice cover estimates derived from CALIOP measurements from June 2006 to June 2016 can be used as an important predictor of sea ice cover and climate change. These figures show monthly time-series plot of the Arctic sea ice extent and area during the period of 1978 to 2016 from three different sources: the red curves show CALIOP measurements (2006–2016), the blue curves show the NASA team algorithm data (1978–2016) and green curves show the AMSR-E dataset (2002 − 2011). For these figures, the CALIOP sea ice extent is computed by the integrated sum of the areas of grid cells with at least 15% ice probability. The entire area of any grid cell with at least 15% ice probability is thus considered to contribute to the total ice extent. The CALIOP sea ice area is defined as the integrated sum of the products of the area of each grid cell with at least 15% ice probability and the corresponding ice probability within the grid cell. Since CALIOP provides observations up to 82°N, the sea ice probability above 82°N was assumed to be 90% for all seasons. The CALIOP sea ice extent and area show excellent agreement with the NASA team and AMSR-E results during the overlap period with the coefficient of determination (R^2) and root mean squared error (RMSE) shown in Table 4. The minor differences between CALIOP and NASA Team (or AMSR-E) results are primarily due to the small number of observations in (0.5° × 1°) of the latitude–longitude grid cell and the assumption of 90% sea ice cover at latitudes >82°N. For example, Fig. 10 shows that the AMSR-E sea ice concentrations above 82°N can vary from 70% to 100% from summer to winter.

Results of Figs. 12 and 13 show that the temporal variations in the monthly averages are dominated by the large seasonality of the ice cover that fluctuates from minimum values in September to maximum values in February or March. The extent of Arctic sea ice reached its new minimum in history in September 2012, measuring 3.56×10^6 km^2 from CALIOP, and 3.63×10^6 km^2 from NASA team. The result that Arctic sea ice extent in September 2012 fell to the lowest value ever recorded agrees with the sea ice extent results generated from the NSIDC (http://nsidc.org/arcticseaicenews/charctic-interactive-sea-ice-graph/).

The CALIOP September sea ice extents in 2006 (pink line) and 2012 (green line) are given in Fig. 14, showing the sea ice extent shrinking from 2006 to 2012. Fig. 14 also presents SSMIS monthly sea ice concentration (%) in September 2012. The results of Fig. 14 indicate that the CALIOP sea ice extent (green line) agrees very well with the SSMIS sea

Table 3
Averaged area fraction of different surface types in four seasons of 2010.

Surface type	Winter	Spring	Summer	Fall
CALIOP Sea ice (%)	70 ± 4	71 ± 6	42 ± 12	38 ± 15
CALIOP Open water (%)	17 ± 1	20 ± 6	38 ± 9	40 ± 13
AMSR-E sea ice (%)	71 ± 5	75 ± 4	46 ± 13	40 ± 13
CALIOP snow/ice cover over land (%)	97 ± 1	80 ± 25	13 ± 6	57 ± 36
MODIS snow cover (%)	98 ± 1	82 ± 21	17 ± 6	56 ± 34

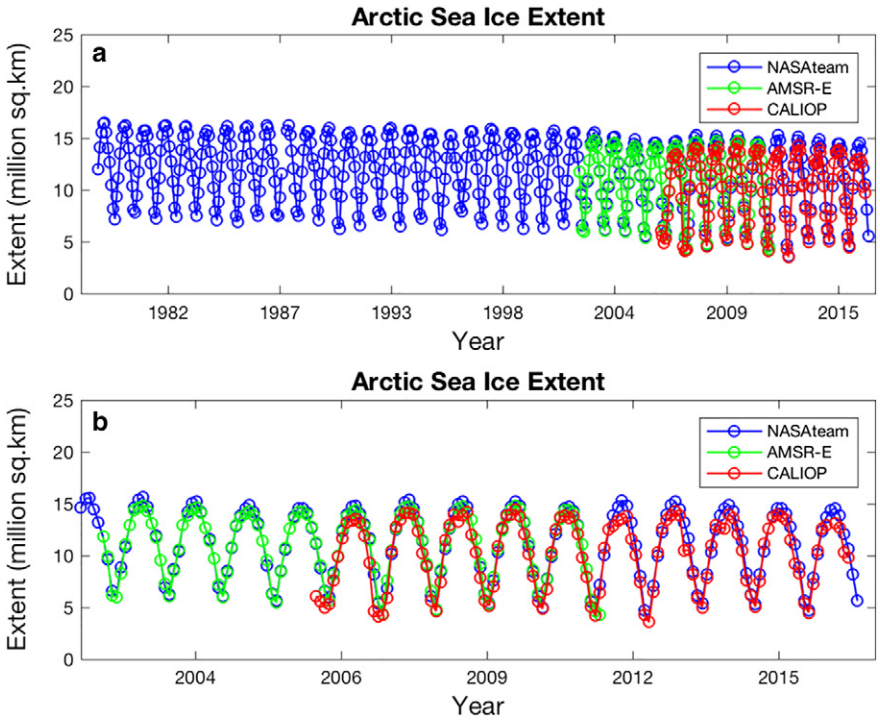

Fig. 12. Upper panel (a): Monthly time-series plot of the Arctic sea ice extent (10^6 km^2) during the period of 1978 to 2016. The bottom panel (b) is for the 2002–2016 time series. Red results are derived from CALIOP lidar measurements (2006–2016), blue results are from the NASA team algorithm data (1978–2016) and green results are from the AMSR-E dataset (2002–2011).

ice extent in September 2012, except the region with longitude from 10° E to about 110° E where there are no CALIOP observations at latitude >82° N. The trend in Arctic September sea ice extent and area from 1979 to 2015 is shown in Fig. 15 with red line representing CALIOP results (2006–2015), blue line representing the NASA team results (1979–2015) and green line representing the AMSR-E results (2002–2011). Table 5 gives the decreasing trend value of Arctic September sea ice extent and area over the 37-year period of the NASA team data

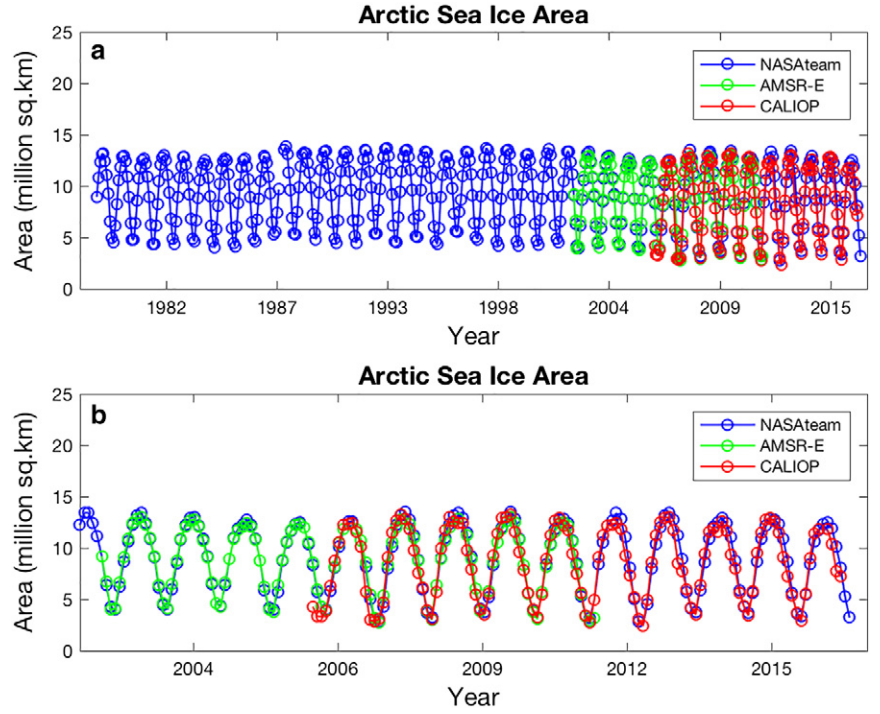

Fig. 13. Upper panel (a): Monthly time-series plot of the Arctic sea ice area (10^6 km^2) during the period of 1978 to 2016. The bottom panel (b) is for the 2002–2016 time series. Red results are derived from CALIOP lidar measurements (2006–2016), blue results are from the NASA team algorithm data (1978–2016) and green results are from the AMSR-E dataset (2002–2011).

Table 4
Summary of comparisons between CALIOP and NASA team results, CALIOP and AMSR-E results, and NASA team and AMSR-E results.

	Sea ice extent		Sea ice area	
	R^2	RMSE (10^6 km^2)	R^2	RMSE (10^6 km^2)
CALIOP vs. NASA Team	0.89	1.10	0.93	0.94
CALIOP vs. AMSR-E	0.87	1.25	0.92	1.03
NASA Team vs. AMSR-E	0.98	0.41	0.99	0.33

and 10-year period of CALIOP measurements. The September sea ice extent reveals a decreasing trend of −42,900 km^2/year for period from 1979 to 1999, and −131,100 km^2/year for period from 2000 to 2015. However, the September sea ice area results reveal a slightly positive increasing trend for period from 1979 to 1999 (10,900 km^2/year) and a decreasing trend for period from 2000 to 2015 (−81,300 km^2/year). The 10-year CALIOP measurements (2006–2015) also show a decreasing trend of September sea ice extent (−33,000 km^2/year) and area (−44,200 km^2/year). For comparison, the corresponding 10-year September sea ice trends from NASA team data are about −43,200 km^2/year and −3800 km^2/year (Table 5), respectively. The results here indicate that the decline in September sea ice cover becomes steeper with time later into the 21st century, which is consistent with many models' results showing an accelerating decline in the summer minimum sea ice extent during the 21st century and reaching a September nearly sea ice free Arctic in the year 2037 (Wang and Overland, 2009, Notz and Stroeve, 2016).

4.2. Case study on cloudy sky

CALIOP provides surface measurements during both daytime and nighttime over a broad range of atmospheric conditions (penetrating significant cloud, fog and aerosol cover). Fig. 16 presents CALIOP surface type identification results on March 1st, 2015 (left panel) and Aug 4th, 2015 (right panel) with the blue dots representing the open water; black dots representing bare ground; red dots representing snow/sea ice surface and green ones representing melting surfaces. The results on left panel of Fig. 16 are from night time measurements while the results on right panel are from day time measurements. For the CALIOP results shown in Fig. 16, both the clear sky cases and cloudy sky cases with cloud optical depths up to 1 are analyzed. The cloud optical depths are from CALIOP level 2 cloud layer products. For comparison with CALIOP surface results, the SSMIS sea ice concentration (%) on March 1st, 2015 (left panel) and Aug 4th, 2015 (right panel) are shown as the background color of Fig. 16. Moreover, we also use results from NASA Goddard Space Flight Center's (GSFC) Slope Imaging Multi-Polarization Photon-counting Lidar (SIMPL), which was deployed on a Langley Research Center (LaRC) King Air to address how both green and infrared wavelength light is affected by water or melt on the ice surface. NASA Jet Propulsion Laboratory's (JPL) Airborne Visible/Infrared Imaging Spectrometer-Next Generation (AVIRIS-NG) was designed to determine how snow-grain size may affect the propagation of green wavelength light. A nadir looking frame camera was also deployed on the NASA LaRC king Air to provide ground validation of returned surface types (Brunt et al., 2015). Fig. 17 shows the mission SIMPL/AVIRIS-NG coordinated science flights that were parallel to the northwest coast of Greenland on Aug 4th, 2015 (Brunt et al., 2015).

In early spring shown in Fig. 16a, the CALIOP retrieved snow/ice surface (red dot) is the dominant surface type, which corresponds to high value (>90%) of SSMIS sea ice concentration. However, CALIOP results show melting green dots (e.g. over Baffin Bay) but SSMIS provides a high value of sea ice concentration there. This could be due to the different horizontal resolutions of CALIOP active lidar and SSMIS passive microwave sensor. CALIOP has a 70 m footprint on Earth every 333 m along ground track while the spatial resolution of SSMIS passive

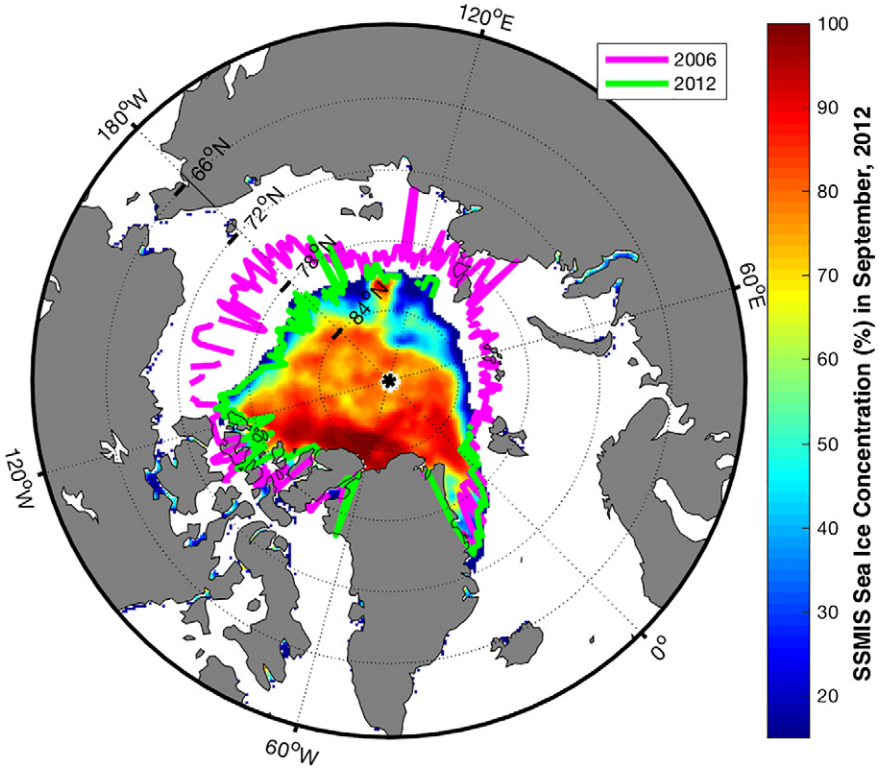

Fig. 14. CALIOP September sea ice extent at year 2006 (pink line) and 2012 (green line) and SSMIS monthly sea ice concentration (%) in September 2012 (color bar).

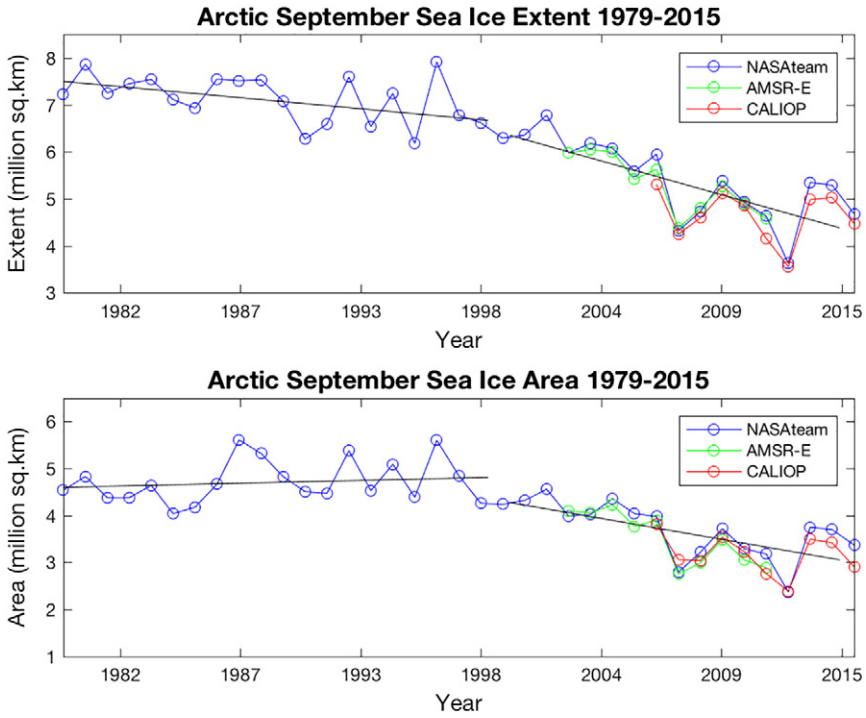

Fig. 15. The Arctic September sea ice cover trends from 1979 to 2015 with red line for CALIOP results (2006–2015), blue line for the NASA team results (1978–2015) and green line for the AMSR-E results (2002–2011).

microwave sensor is 25 km by 25 km, and thus cannot resolve small scale changes in surface conditions. For the summer results shown in Fig. 16b, snow is completely melted over some land surfaces so that bare grounds (black dots) appear. Open water (blue dots) is the dominant type over Kara and Barents Seas and Baffin Bay, corresponding to SSMIS sea ice free region. Sea ice (red dots) still remains in the high latitude region of the Arctic Ocean, corresponding to high value of SSMIS sea ice concentration. There are still snow surfaces over Greenland with melting near the coast area. Compared with CALIOP retrieved surface types, the SIMPL/AVIRIS-NG mission on Aug 4th 2015 also found surface types of coast melt pond over cloud free regions, snow surface, bare ground and open water with light clouds cover over central stretch (Brunt et al., 2015). This shows the ability of CALIOP to provide meaningful additional information in cloudy conditions. A more in-depth study on the accuracy of CALIOP retrieved surface types in non-clear sky conditions will be done in future.

5. Summary and conclusions

In this study, we developed a robust method to monitor snow and sea ice cover in the Arctic using CALIOP measurements. The method takes advantage of the spectral differences of snow/ice reflectance in the visible and near infrared wavelengths to identify snow/ice versus other features in a lidar footprint. Spectral snow/ice reflectance is typically highest in the visible wavelengths and drops off in the near infrared wavelengths, while other land surface covers, such as bare soil, grass, trees, concrete, or asphalt generally show a steady rise in reflectance as wavelength increases from the visible to the near infrared. This characteristic results in different relationships between integrated attenuated backscatter color ratio and depolarization ratio for the snow/ice covered surface, surface melting, open water and land surfaces. This new technique takes advantage of these relationships to distinguish among several different surface types.

To validate the new method, the CALIOP retrieved results have been compared with the results from MODIS/Aqua, NASA team and AMSR-E datasets. Comparison results demonstrate that the new method can effectively detect the Arctic snow and sea ice cover. The CALIOP retrieved snow/ice coverage over land is in good agreement with the MODIS snow cover with a correlation coefficient of 0.92. The CALIOP Arctic sea ice results compare excellently with results from the NASA team and AMSR-E data, with the coefficient of determination higher than 0.8 and RMSE $<1.3 \times 10^6$ km^2. CALIOP retrieved results from its 10 years of observations can be used as the basis for creating an enhanced historical sea ice data set that can be used for sea ice cover variability and trend studies. Compared with the trend of Arctic sea ice cover change during 1979–1999, the September sea ice cover shows an accelerating decline during 2000–2015 with the new extreme minimum observed in 2012.

The launch of CALIOP lidar provides the opportunity to study the sea ice cover at a higher temporal (both daytime and nighttime) and spatial resolution (about 70 m footprint size) than was previously available from passive sensors. The Arctic sea ice cover retrieved from CALIOP lidar and other passive microwave sensors will increase our ability to forecast the future of the sea ice cover. CALIOP provides measurements during both day and night at low solar angles and through considerable aerosol loads and thin clouds making it a reliable source of dataset for the Arctic snow and sea ice studies, which are important climate indicator in glaciology research. Our future study will focus on the accuracy of CALIOP retrieved surface types in other weather conditions to validate

Table 5
Trends in the Arctic September Sea ice covers during the period 1979–2015.

Year	Extent slope (10^6 km^2/year)	Area slope (10^6 km^2/year)
1979–1999	−0.0429	0.0109
2000–2015	−0.1311	−0.0813
NASA Team: 2006–2015	−0.0432	−0.0038
CALIOP:2006–2015	−0.0330	−0.0442

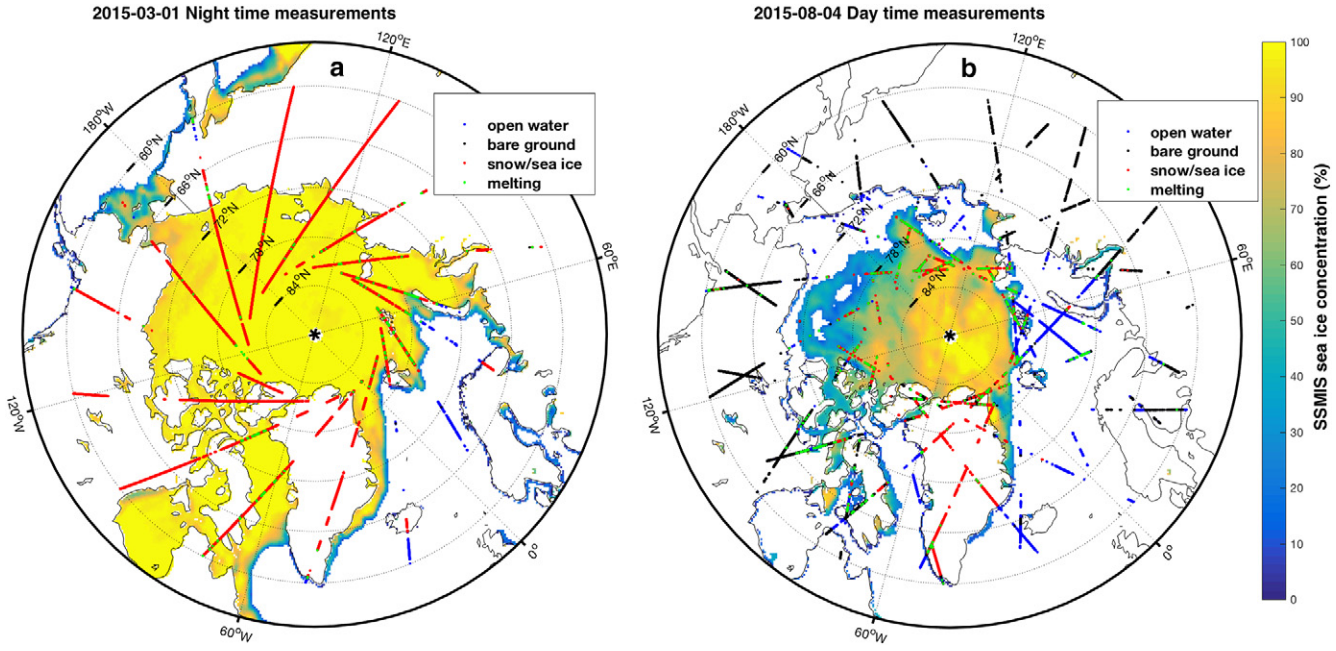

Fig. 16. Surface type identification from CALIOP lidar measurements on March 1st, 2015 (left panel) and Aug 4th, 2015 (right panel). Blue dots: open water; black dots: bare ground; red dots: snow/sea ice surface; green dots: melting surface. Background color is the SSMIS sea ice concentration (%) on March 1st, 2015 (left panel) and Aug 4th, 2015 (right panel).

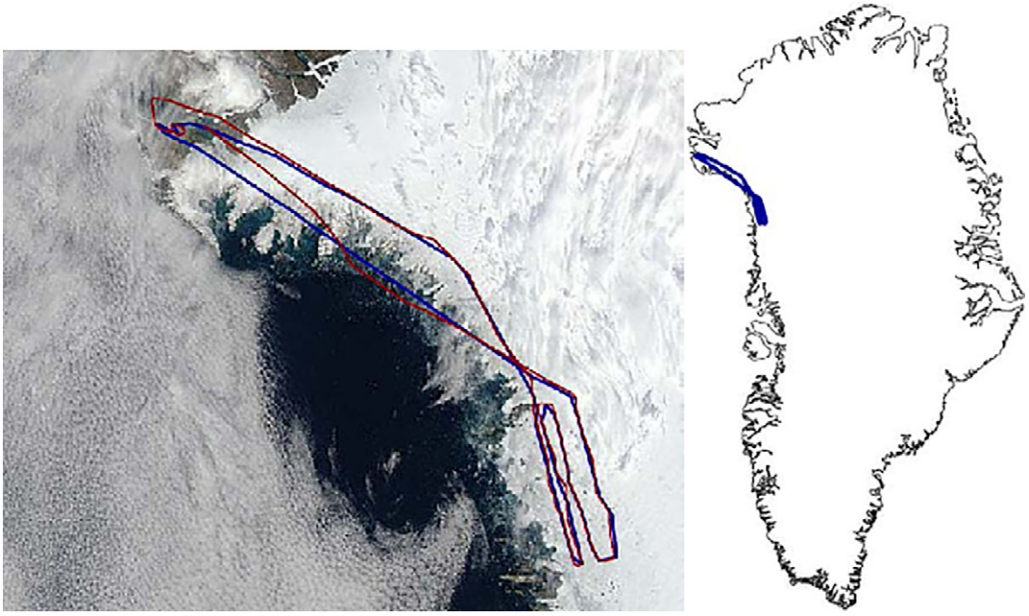

Fig. 17. Mission: SIMPL & AVIRIS-NG coordinated science flights on Aug 4, 2015. Red track: SIMPL; Blue track: AVIRIS-NG (Brunt et al., 2015).

the surface type in cloudy sky conditions with cloud optical depth ranging up to 3.

Acknowledgements

We thank the National Snow and Ice Data Center (NSIDC) for providing the NASA team sea ice trends data and AMSR-E daily sea ice concentration data. CALIPSO is a NASA-CNES mission and we thank both institutions for their support. This study is sponsored by NASA CALIPSO/CloudSat Science Team and supported from David Considine of NASA Headquarter.

References

http://ceres.larc.nasa.gov/science_information.php?page=CeresSurfID (accessed on 01/04/2017).
https://lta.cr.usgs.gov/GTOPO30 (accessed on 01/04/2017).
http://nsidc.org/arcticseaicenews/charctic-interactive-sea-ice-graph/ (accessed on 01/04/2017).
http://nsidc.org/data/smmr_ssmi_ancillary/index.html (accessed on 01/04/2017).
Behrenfeld, M.J., Hu, Y., Hostetler, C.A., Dall'Olmo, G., Rodier, S.D., Hair, J.W., Trepte, C.R., 2013. Space-based lidar measurements of global ocean carbon stocks. Geophys. Res. Lett. 40:4355–4360. http://dx.doi.org/10.1002/grl.50816.
Brunt, K.M., Neumann, T.A., & Markus, T. (2015). SIMPL/AVIRIS-NG Greenland 2015; flight report. NASA Technical Memorandum, 217544. Available from https://ntrs.nasa.gov/archive/nasa/casi.ntrs.nasa.gov/20160012306.pdf (accessed on 01/29/2017).

Cavalieri, D.J., Markus, T., Comiso, J.C., 2014. AMSR-E/Aqua Daily L3 12.5 km Brightness Temperature, Sea Ice Concentration, & Snow Depth Polar Grids, Version 3. NASA National Snow and Ice Data Center Distributed Active Archive Center, Boulder, Colorado USA http://dx.doi.org/10.5067/AMSR-E/AE_SI12.003.

Dozier, J., 1989. Spectral signature of alpine snow cover from the Landsat thematic mapper. Remote Sens. Environ. 28:9–22. http://dx.doi.org/10.1016/0034-4257(89)90101-6.

Fetterer, F., Knowles, K., Meier, W., Savoie, M., 2016. Updated daily. Sea Ice Index, Version 2. Ice Extent and Area. NSIDC: National Snow and Ice Data Center, Boulder, Colorado, USA http://dx.doi.org/10.7265/N5736NV7 [09/15/2016 Accessed].

Gao, B.-C., Han, W., Tsay, S.C., Larsen, N.F., 1998. Cloud detection over the Arctic region using airborne imaging spectrometer data during the daytime. Journal of Applied Meteorology 37, 1421–1429 (10.1175/1520-0450(1998)037<1421:CDOTAR>2.0.CO;2).

Goetz, S., Huemmrich, F., 2003. Plant and vegetation community properties. Chapter 4. In: Russell, Carol, Hart, Jay (Eds.), Global Land Vegetation-An Electronic Textbook http://www.ccpo.odu.edu/SEES/veget/vg_class.htm (accessed on 01/04/2017).

Hall, D.K., Riggs, G.A., 2007. Accuracy assessment of the MODIS snow products. Hydrol. Process. 21:1534–1547. http://dx.doi.org/10.1002/hyp.6715.

Hall, D.K., Riggs, G.A., Salomonson, V.V., DiGirolamo, N.E., Bayr, K.J., 2002. MODIS snow-cover products. Remote Sens. Environ. 83:181–194. http://dx.doi.org/10.1016/S0034-4257(02)00095-0.

Hall, D.K., Riggs, G.A., Salomonson, V.V., 2007. Updated daily. MODIS/Aqua Snow Cover Daily L3 Global 500m Grid V005, National Snow and Ice Data Center. Digital media; Boulder, Colorado USA.

Hu, Y., Powell, K., Vaughan, M., Tepte, C., Weimer, C., Beherenfeld, M., Young, S., Winker, D., Hostetler, C., Hunt, W., Kuehn, R., Flittner, D., Cisewski, M., Gibson, G., Lin, B., MacDonnell, D., 2007. Elevation information in tail (EIT) technique for lidar altimetry. Opt. Express 15:14504–14515. http://dx.doi.org/10.1364/OE.15.014504.

Hu, Y., Stamnes, K., Vaughan, M., Pelon, J., Weimer, C., Wu, D., Cisewski, M., Sun, W., Yang, P., Lin, B., Omar, A., Flittner, D., Hostetler, C., Trepte, C., Winker, D., Gibson, G., Santa-Maria, M., 2008. Sea surface wind speed estimation from space-based Lidar measurements. Atmos. Chem. Phys. 8 (13):3593–3601. http://dx.doi.org/10.5194/acp-8-3593-2008.

Hunt, W.H., Winker, D.M., Vaughan, M.A., Powell, K.A., Lucker, P.L., Weimer, C., 2009. CALIPSO Lidar description and performance assessment. J. Atmos. Oceanic Tech. 26: 1214–1228. http://dx.doi.org/10.1175/2009JTECHA1223.1.

Josset, D., Pelon, J., Hu, Y., 2010a. Multi-instrument calibration method based on a Multi-wavelength Ocean surface model. IEEE Geosci. Remote Sens. Lett. 7:195–199. http://dx.doi.org/10.1109/lgrs.2009.2030906.

Josset, D., Pelon, J., Hu, Y., Zhai, P.-W., Powell, K., Rodier, S., Trepte, C., 2010b. CALIPSO Land Surface Mapping Principle and First Results. 1316–1319 in 25th International Laser Radar Conference (ILRC) (St. Petersburg, Russia).

Josset, D., Zhai, P.-W., Hu, Y., Pelon, J., Lucker, P.L., 2010c. Lidar equation for ocean surface and subsurface. Opt. Express 18:20862–20875. doi.org/10.1364/OE.18.020862.

Josset, D., Pelon, J., Garnier, A., Hu, Y., Vaughan, M., Zhai, P.-W., Kuehn, R., Lucker, P., 2012. Cirrus optical depth and lidar ratio retrieval from combined CALIPSO-CloudSat observations using ocean surface echo. J. Geophys. Res. Atmos. 117:1–14. http://dx.doi.org/10.1029/2011JD016959.

König, M., Winther, J.-G., Isaksson, E., 2001. Measuring snow and glacier ice properties from satellite. Rev. Geophys. 39:1–27. http://dx.doi.org/10.1029/1999RG000076.

Lemke, P., Ren, J., Alley, R.B., Allison, I., Carrasco, J., Flato, G., Fujii, Y., Kaser, G., Mote, P.W., Thomas, R.H., Zhang, T., 2007. Observations: changes in snow, ice and frozen ground. Chapter 4. In: Solomon, S., Qin, D., Manning, M., Chen, Z., Marquis, M., Averyt, K.B., Tignor, M., Miller, H.L. (Eds.), Climate Change 2007: the Physical Science Basis. Contribution of Working Group I to the Fourth Assessment Report of the Intergovernmental Panel on Climate Change. Cambridge University Press, Cambridge, United Kingdom and New York, NY, USA.

Liang, S., Shuey, C.J., Russ, A.L., Fang, H., Chen, M., Walthall, C.L., Daughtry, C.S.T., Hunt Jr., R., 2003. Narrowband to broadband conversions of land surface albedo: II. Validation. Remote Sens. Environ. 84:25–41. http://dx.doi.org/10.1016/S0034-4257(02)00068-8.

Lu, X., Hu, Y., Trepte, C., Zeng, S., Churnside, J.H., 2014. Ocean subsurface studies with the CALIPSO spaceborne lidar. J. Geophys. Res. Oceans 119:4305–4317. http://dx.doi.org/10.1002/2014jc009970.

Lu, X., Hu, Y., Pelon, J., Trepte, C., Liu, K., Rodier, S., Zeng, S., Lucker, P., Verhappen, R., Wilson, J., Audouy, C., Ferrier, C., Haouchine, S., Hunt, B., Getzewich, B., 2016. Retrieval of ocean subsurface particulate backscattering coefficient from space-borne CALIOP lidar measurements. Opt. Express 24 (25):29001–29008. http://dx.doi.org/10.1364/OE.24.029001.

Markus, T., Cavalieri, D.J., 2000. An enhancement of the NASA Team Sea ice algorithm. IEEE Trans. Geosci. Remote Sens. 38:1387–1398. http://dx.doi.org/10.1109/36.843033.

Markus, T., Cavalieri, D.J., Ivanoff, A., 2011. Algorithm theoretical basis document for the AMSR-E sea ice algorithm. Revised December 2011. Goddard Space Flight Center, Landover, MD https://nsidc.org/sites/nsidc.org/files/technical-references/amsr-atbd-supp12-seaice.pdf (accessed on 01/19/2017).

Mortin, Jonas, Svensson, Gunilla, Graversen, Rune G., Kapsch, Marie-Luise, Stroeve, Julienne C., Boisvert, Linette N., 2016. Melt onset over Arctic Sea ice controlled by atmospheric moisture transport. Geophys. Res. Lett. 43 (12):6636–6642. http://dx.doi.org/10.1002/2016GL069330.

Notz, Dirk, Stroeve, Julienne, 2016. Observed Arctic Sea-ice loss directly follows anthropogenic CO_2 emission. Science http://dx.doi.org/10.1126/science.aag2345.

Parajka, J., Holko, L., Kostka, Z., Blöschl, G., 2012. MODIS snow cover mapping accuracy in a small mountain catchment - comparison between open and forest sites. Hydrol. Earth Syst. Sci. 16:2365–2377. http://dx.doi.org/10.5194/hess-16-2365-2012.

Perovich, D.K., Polashenski, C., 2012. Albedo evolution of seasonal Arctic sea ice. Geophys. Res. Lett. 39, L08501. http://dx.doi.org/10.1029/2012gl051432.

Perovich, D.K., Grenfell, T.C., Light, B., Hobbs, P.V., 2002. Seasonal evolution of the albedo of multiyear Arctic sea ice. J. Geophys. Res. Oceans 107:8044. http://dx.doi.org/10.1029/2000jc000438.

Perovich, D.K., Light, B., Eicken, H., Jones, K.F., Runciman, K., Nghiem, S.V., 2007. Increasing solar heating of the Arctic Ocean and adjacent seas, 1979–2005: attribution and role in the ice-albedo feedback. Geophys. Res. Lett. 34, L19505. http://dx.doi.org/10.1029/2007gl031480.

Persson, P., 2012. Onset and end of the summer melt season over sea ice: thermal structure and surface energy perspective from SHEBA. climate Dynam. 39 (6), 1349–1371.

Stroeve, J., 2003. Sea ice trends and climatologies from SMMR and SSM/I-SSMIS, version 1-total ice area extent. NASA National Snow and Ice Data Center Distributed Active Archive Center, Boulder, Colorado USA http://dx.doi.org/10.5067/C2HMG48G83QQ [09/15/2016 accessed].

Wang, M., Overland, J.E., 2009. A sea ice free summer Arctic within 30 years? Geophys. Res. Lett. 36, L07502. http://dx.doi.org/10.1029/2009gl037820.

Warren, S.G., 1982. Optical properties of snow. Rev. Geophys. 20:67–89. http://dx.doi.org/10.1029/RG020i001p00067.

Winker, D.M., Vaughan, M.A., Omar, A., Hu, Y., Powell, K.A., Liu, Z., Hunt, W.H., Young, S.A., 2009. Overview of the CALIPSO mission and CALIOP data processing algorithms. J. Atmos. Oceanic Tech. 26:2310–2323. http://dx.doi.org/10.1175/2009jtecha1281.1.

Winker, D.M., Pelon, J., Coakley, J.A., Ackerman, S.A., Charlson, R.J., Colarco, P.R., Flamant, P., Fu, Q., Hoff, R.M., Kittaka, C., Kubar, T.L., Le Treut, H., McCormick, M.P., Mégie, G., Poole, L., Powell, K., Trepte, C., Vaughan, M.A., Wielicki, B.A., 2010. The CALIPSO mission: A global 3D view of aerosols and clouds. Bull. Am. Meteorol. Soc. 91:1211–1229. http://dx.doi.org/10.1175/2010bams3009.1.

Winther, J.-G., Edvardsen, K., Gerland, S., Hamre, B., 2004. Surface reflectance of sea ice and under-ice irradiance in Kongsfjorden, Svalbard. Polar Res. 23:115–118. http://dx.doi.org/10.1111/j.1751-8369.2004.tb00134.x.

Wolff, E.W., 2013. Ice Sheets and Nitrogen. Biological Sciences, Philosophical Transactions of the Royal Society of London B:p. 368 http://dx.doi.org/10.1098/rstb.2013.0127.